

Estimation of the temperature in the stirred zone and cooling Rate of friction stir welding of EH46 Steel from TiN Precipitates

AL-MOUSSAWI, Montadhar, SMITH, Alan <<http://orcid.org/0000-0001-7868-8501>>, FARAJI, Masoumeh and CATER, Stephen

Available from Sheffield Hallam University Research Archive (SHURA) at:

<https://shura.shu.ac.uk/24994/>

This document is the Accepted Version [AM]

Citation:

AL-MOUSSAWI, Montadhar, SMITH, Alan, FARAJI, Masoumeh and CATER, Stephen (2019). Estimation of the temperature in the stirred zone and cooling Rate of friction stir welding of EH46 Steel from TiN Precipitates. Metallurgical and Materials Transactions A. [Article]

Copyright and re-use policy

See <http://shura.shu.ac.uk/information.html>

1 Estimation of the Temperature in the Stirred Zone and Cooling Rate of 2 Friction Stir Welding of EH46 Steel from TiN Precipitates

3 *Montadhar Al-moussawi, ** Alan J. Smith, ***¹ Masoumeh Faraji, **** Stephen Cater,

4
5 Al-Furat Al-Awsat university, Iraq; **Sheffield Hallam University, Sheffield, S1 1WB, UK; ***Coventry
6 University, Coventry, CV1 2JH, UK; **** TWI Yorkshire Technology Centre, Rotherham, S60 5TZ, UK
7 Corresponding email: masoumeh.faraji@coventry.ac.uk

8 9 **Abstract**

10 Measuring the peak temperature in the contact region of the tool/workpiece in friction stir
11 welding (FSW) is difficult using conventional methods such as use of thermocouples or a
12 thermal imaging camera, hence an alternative method is required to tackle this problem. The
13 objective of the present work was to estimate more accurately, for the first time, the peak
14 temperature and cooling rate of FSW from precipitation of TiN in friction stir welded steel
15 samples. Microstructures of nine friction stir welded samples of high strength shipbuilding
16 steel of EH46 grade were examined closely by SEM-EDS to detect the TiN precipitates.
17 Thermal heat treatments using an accurate electrical digital furnace were also carried out on
18 80 unwelded EH46 steel samples over a range of temperatures and cooling rates. Heat
19 treatments were to create a basis to understand TiN precipitation behavior under various
20 heating and cooling regimes for the studied alloy. Heat treatment showed that TiN particles
21 can precipitate at a peak temperature exceeding 1000°C and the size of TiN precipitates
22 particles increases with decreasing cooling rate. In a temperature range between 1100-1200°C
23 the TiN precipitates were accompanied by other elements such as Nb, S, Al and V. Pure TiN
24 particles were found after the peak temperature exceeded 1250°C with limited precipitation
25 after reaching a peak temperature of 1450°C. The comparison between the friction stir
26 welding samples and the heat treatments in terms of types and sizes of TiN precipitates
27 suggests that the welding peak temperature should have been in the range of 1200-1350°C
28 with a cooling rate in the range of 20-30 K/sec. The current work represents a step change in
29 estimating the friction stir welding temperature and cooling rate which are difficult to
30 determine using thermocouples and thermal imaging camera.

31
32 **Keywords: Friction Stir Welding (FSW), EH46 steel, TiN precipitates, Peak**
33 **temperature, Cooling rate.**

34 35 **1-Introduction**

36 Friction stir welding (FSW) which was invented in the UK/TWI in 1991 [1] is still a
37 challenge when utilized for high melting alloys such as steel. In addition to the high cost of
38 the tools, the prime challenge is to select suitable welding parameters to produce sound welds.
39 The most important factor in the FSW process is to find the right temperature required to
40 make the steel yield under specific tool rotational and traverse speeds during welding.
41 Determination of this temperature in the workpiece/tool contact region during friction stir
42 welding is usually difficult. Thermocouples (TC_s) which are usually used for this purpose
43 cannot be placed directly in the stir zone region because they will be damaged or displaced by
44 the deforming material in the stir zone before recording the peak temperature, leading to
45 inaccurate measurements. Moreover, thermocouples attached to the top surface adjacent to
46 the edge of the stir zone are often severed by extrusion of the flash from under the tool
47 shoulder before reaching peak temperature. An earlier study has used thermocouples to
48 measure the temperature of the contact region for friction stir welding of an aluminum alloy
49 (AA6061-T6) [2]. They have, however, drilled eight holes with 1.5 mm diameters at different
50 positions of the work-piece to insert TCs. Using a thermal imaging camera for measuring the
51 temperature of work-piece during FSW is also difficult and cannot produce accurate data.

52 This is because the field of view of the camera can be restricted by the presence of the argon
53 gas shield applied to the weld area, and the presence of clamps that is holding down the
54 workpiece. The camera also has no direct view of the tool itself, and measuring the
55 temperatures on the surface of the plate adjacent to the weld area, using camera, gives data
56 that are unrepresentative of the internal weld temperatures. Finally, the emissivity of the tool
57 can change significantly during the weld process and thus accurate calibration of the camera
58 is also another significant drawback.

59 Elsewhere Carlone and Palazzo [3] have used an infrared thermal camera, fixed on the
60 machine and focused on the leading edge, to determine the surface temperature of the weld in
61 an AA2024-T3 alloy. However, they have not discussed the reproducibility and level of
62 precision of their measurements. For the rotational (ω) and traverse (v) speeds of 800 rpm
63 and 140 mm/min they have reported a peak temperature of 475°C. More recently Mezyk and
64 Kowieski [4] have used short wave infrared camera mounted on the FSW mill to detect
65 discontinuities in the FSW workpieces and also to monitor the temperature. They have
66 reported appearance of excessive “burr” on both sides of the weld where part of the burr (a
67 shaving) was pushed out behind the tool which caused disturbances on thermograms
68 (camera’s recorded data); such disturbances caused a jump of 100°C in the temperature
69 profile along the measurement line. Hence, they described this technique as a qualitative
70 method which still needs further development.

71 Compared to direct temperature measurements, using an analytical approach, Zhang et al [5]
72 have used the equation developed by Arora et al [6], presented below, to calculate the peak
73 temperature (T , °C) in FSW of AA2024-T3 alloys.

74

$$75 \quad T = (0.151 \log_{10} \left(\frac{\sigma_8 A \omega C \eta}{\lambda v^2} \right) + 0.097) (T_s - T_r) + T_r \quad (1)$$

76 where T_s is the solidus temperature, T_r is the initial temperature, ω and v are rotational and
77 traverse speeds, σ_8 is the yield stress of the material at a temperature of $0.8T_s$, A is the cross-
78 sectional area of the tool shoulder, C and λ are the specific heat capacity and thermal
79 conductivity of the workpiece material, respectively, and η is the ratio of generated heat at the
80 shoulder/workpiece interface, transported between the tool and the workpiece.

81 They have estimated the peak temperature under welding speeds of ω and v of 800 rpm and
82 140 mm/min to be 455°C. Moreover, Wang et al [7] measured the peak temperature of FSW
83 plates of AA2024-T4 using thermocouples. They have reported peak temperature of 425°C
84 for ω and v of 750 rpm and 150 mm/min. These conditions are very similar to the above-
85 mentioned study where thermal camera has been used to measure the peak temperature,
86 however, the reported peak temperature measured using thermal camera is significantly
87 higher. Therefore, the reliability of thermal camera for FSW temperature measurements
88 should be questioned.

89 In the present work, the use of a new off-line method which depends on the formation of TiN
90 precipitates during the heating-cooling cycle of FSW is investigated. Clearly, the existence of
91 TiN particles is dependent on the process of as-received materials. TiN particles are
92 diminished at faster cooling rates during solidification [8]. This method is to enable a more
93 accurate estimation of the peak temperature at the interface as well as cooling rate of the
94 sample after the welding is completed. It is also an accurate and inexpensive alternative
95 method compared with the use of thermocouples and thermal imaging camera.

96 In order to use the suggested off-line method, it is of paramount importance to understand
97 how and when TiN particles precipitate and appear in steel grades, particularly in low alloy
98 grades similar to the grade used in this work. Precipitation of TiN during heating and cooling
99 cycles in various steel grades have been studied previously mostly during solidification, pre-
100 deformation heating and post deformation. Stock et al. [8] investigated the cooling rate
101 effects on TiN precipitates in low carbon steel during and after solidification and found that

102 TiN particles can precipitate at very high temperatures near the melting point of the steel.
103 They also found that TiN particles size increases with decreasing cooling rates and the
104 precipitate size can reach 1-2.5 μm at low cooling rates (0.1 K/s), whereas, particles tend to
105 cluster for higher cooling rates (600 K/s). Nagata et al. [9] studied the TiN particles
106 distribution in a thin-slab cast HSLA steel grade (similar to the grade studied here) using
107 TEM examination. They found that TiN precipitate size decreased with increasing post
108 solidification cooling rate. Using TEM and electrolytic chemical analysis and focusing on
109 formation temperature of Ti particles El-Fawakhry et al. [10] studied TiN precipitation in
110 microalloyed steels with Ti, subjected to hot rolling. They found TiN precipitates of 5-10 μm
111 in samples taken from alloys hot rolled at 1250°C. It is believed that due to high stability of
112 TiN, it precipitates at very high temperatures, most probably in the molten state as coarse
113 precipitates. Wang et al. [11] found that in low carbon steel the TiN particles nucleated on
114 Ti_2O_3 -particles. Hong et al. [12] studied the evolution of precipitates in Nb-V-Ti
115 microalloyed steel in a temperature range of 1100-1400°C using TEM. Their study found that
116 (Ti,Nb)(C,N) carbonitrides disappeared after reheating the alloy in a temperature range
117 higher than 1000°C and a new cubic shape particles precipitated in the microstructure with a
118 size depending on the peak temperature and cooling rate. They found that as reheating
119 temperature increased from 1050 to 1400°C, Nb content within precipitates decreased;
120 however, Ti content did not alter till 1250°C and above 1300°C, Ti began to dissolve into the
121 austenite matrix. All these studies [10-12] suggest that in low carbon low alloy steel, TiN
122 won't dissolve in temperatures below 1200°C. In alloys similar to the grade studied here, this
123 can provide a basis for a minimum temperature above which TiN can be found.
124 The current study aims to identify TiN precipitates in the microstructure of samples taken
125 from stirred zones of FS welded of high strength shipbuilding EH46 steel plates using SEM-
126 EDS. Such precipitates are to be compared with precipitates formed in heat treated un-welded
127 samples of the same steel grade with the same thickness. Heat treatments are conducted under
128 various thermal and cooling regimes to enable simulation of various peak temperatures and
129 cooling rates of the welded counterparts.

130 It is worth noting that, although FSW is a thermomechanical process, the strain rate effect has
131 not been taken into consideration in the heat treatment procedures. However, it is expected
132 that strain rate will influence mainly the incubation time of phase transformation and
133 elemental precipitation/segregation. This theory is supported by previous works carried out
134 on steel where in addition to heat treatments strain rates (using methods such as hot
135 compression, rolling and FSW) were applied. They have shown that the phase changes [13]
136 and elemental precipitation occur faster when the process includes strain rate in addition to
137 the heating; e.g. in microalloyed steels at greater strains, the incubation and completion time
138 for precipitation are shorter ([14-15]). Failla et al. [13] studied the effect of deformation on
139 the phase transformation of ferrite and bainite in HSLA-65 alloy during FSW process and
140 found that phase transformation occurs faster when deformation increases. Upon application
141 of deformation austenite grain size was reduced during the FSW process which promoted the
142 formation of ferrite. The incubation time of Nb(C,N) elemental precipitation has also been
143 studied by Zhu and Qiu [15], in a microalloyed steel during continuous cooling, which was
144 found to decrease with an increase in strain rate. The time of precipitation was reduced from
145 6000 secs to 3548 secs with the casting speed increasing from 0.9m/min to 2.4m/min whereas,
146 the temperature of precipitation onset remained constant [15].

147 The main aim of this work is to implement a simpler method to determine the peak
148 temperatures of EH46 FS welded samples by studying TiN precipitation in this alloy. It is
149 also to produce a known list of few peak temperatures and cooling rates of such steel grade
150 from TiN precipitates sizes. This procedure can be used to select the best tool rotational and

151 traverse speeds that generate desirable temperatures during FSW and thus to control the
 152 process more readily.

153

154 **2-Materials and Methods**

155 The chemical composition (wt%) of EH46, which is an Nb-V microalloyed low Sulphur steel,
 156 as provided by the manufacturer, is shown in Table 1.

157

158 **2.1 FSW Samples**

159 Nine FS welded samples were produced from plates of EH46 grade (14.8 mm thickness) at
 160 TWI Technology Centre in Yorkshire using PowerStir welding machine equipped with Poly
 161 Crystalline Boron Nitride (PCBN) hybrid tool. The tool consisted of a shoulder with a
 162 diameter of 38mm and probe with a length of 12mm. Out of these samples seven specimens
 163 were produced under plunge and dwell welding conditions and the remaining two were
 164 welded under steady state condition. Their positioning is shown in Figure 1. The plunge trial
 165 welds are denoted as W1 to W7 and the steady state trials are coded as W8 and W9. The
 166 welding parameters for the plunge/dwell and steady state conditions are shown in Tables 2
 167 and 3, respectively.

168

169 **Table 1: Chemical composition (wt%) of EH46 Steel Grade as received (composition is
 170 provided by the manufacturer).**

C	Si	Mn	P	S	Al	N	Nb	V	Ti
0.20	0.55	1.7	0.03	0.03	0.015	0.02	0.03	0.10	0.02

171

172

173

174

175

176

177

178

179

180

181

182

183

184

185



Figure 1: Representation of the positioning of the seven plunge trials for EH46 steel plates.

Table 2: The welding parameters for FS welded EH46 plunge/dwell samples (W1-W7).

Weld Trial No.	Tool rotational speed ω (RPM) at dwell period	Max. Axial (Plunge) force (F_z) KN	Max. longitudinal force (F_x) KN	Max. Torque (M) N.m	Plunge Depth (Z) mm from FSW machine	Dwell Time (t) sec at dwell period
W1	200	157	17	498	13	6
W2	200	127	17	471	13	8
W3	120	116	21	598	13	7
W4	120	126	20	549	13	6
W5	120	115	17	532	13	7
W6	120	105	18	583	13	7
W7	120	119	20	548	13	7

186
187
188
189
190

Table 3: Welding parameters for FS welded EH46 steel at steady state condition (W8 and W9).

Weld No.	Tool rotation speed RPM	Traverse speed mm/min	Rotational/ Traverse speeds (rev/mm)	average spindle Torque N.m	average tool Torque N.m	Axial force (average) KN	longitudinal force (average) KN	Representation of Heat Input $(\frac{\omega \times torque}{v})$ (rev. KN)
W8	150	50	3	300	114	66	13	342
W9	150	100	1.5	450	171	72	14	256.5

191
192

2.2 Heat Treated Samples

193
194 Heat treatments were conducted on 80 samples of EH46 steel, each sample was a cube of
195 14.8 mm in length. The heat treatments were carried out in a calibrated electric furnace at
196 temperatures ranging from 1000 to 1500°C and at holding times of approximately 10 to 30
197 sec. Samples were placed in the center of the furnace and the surface temperature of the
198 sample under study was measured by an attached thermocouple connected to a digital 4-
199 channel data logger thermometer. Different cooling rates were applied including quenching in
200 oil (90K/sec), quenching in hot oil with a temperature of 150°C (30K/sec), still air cooling
201 and cooling inside the furnace (0.35K/sec). The values for cooling rates of different media are
202 determined using temperature profile of samples obtained by thermocouples attached to their
203 surface.

204

2.3 SEM - EDS

205
206 Scanning electron microscopy (SEM) examination was carried out on polished and etched
207 (with 2% Nital) friction stir welded and also heat treated samples. SEM produced high
208 quality and high resolution images of micro constituents by employing secondary electron
209 (SE) imaging mode with accelerating voltages of 10 to 20 kV which provides high
210 penetration. The working distance (WD) used was 10 mm but in some cases, it was altered
211 (decreased or increased) to enhance the contrast at higher magnification. Energy Dispersive
212 Spectroscopy EDS (point and ID) based on SEM was used to detect the Ti precipitates. The
213 changes in Prior Austenite Grain Size (PAGS) with temperature have been measured using
214 the linear intercept method (ASTM E-112). To find each average value of PAGS, about 5 to 7
215 images were taken and measured carefully. The TiN particles diameter and their distribution
216 were measured by applying square grid using image grid software in which the number of
217 intersections of the grid falling in the TiN particles were counted and compared with the total
218 number of points laid down. When measuring average size of TiN particles for each
219 condition 7 images were taken separately in dimensions of 600 μm by 600 μm and then they
220 were used in image grid software.

221

222

3-Results

223

3.1 Prior Austenite Grain Size (PAGS) and Temperature

224

225 To understand the role of temperature on the prior austenite grain size (PAGS) Figure 2
226 illustrates the relationship between peak temperature and PAGS for holding time of 30 sec.

227

228
229
230
231
232
233
234
235
236
237
238
239
240
241
242
243
244
245
246
247
248
249
250
251
252
253
254
255
256
257
258
259
260
261
262
263
264
265
266
267
268
269
270
271
272
273
274
275
276

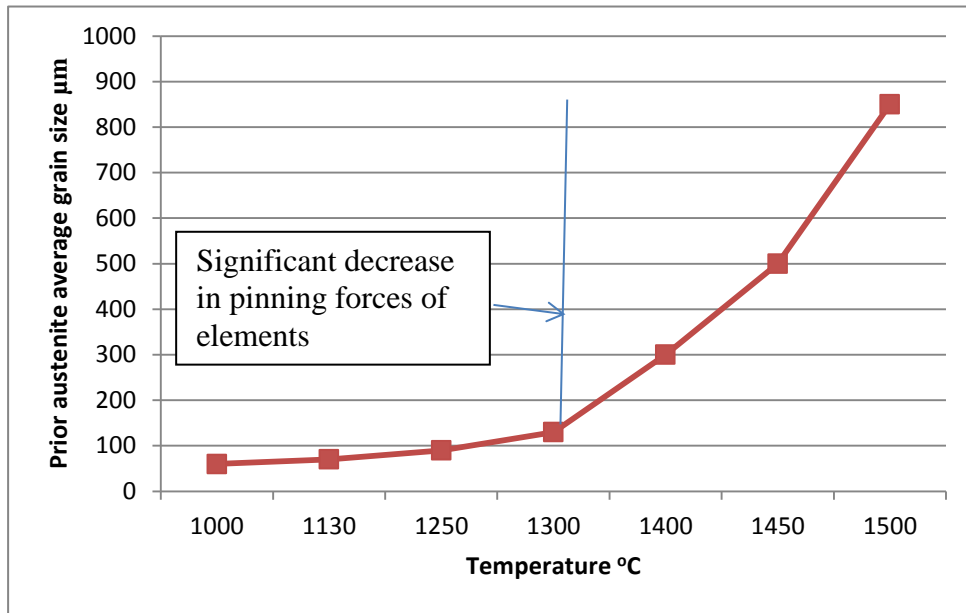


Figure 2: Variation of prior austenite grain size with temperature for heat treated samples of EH46 in temperature range of 1000-1500 °C with holding time of 30sec.

3.2 TiN precipitates in the heat treated samples

Figure 3 is a high magnification SEM image of the as-received EH46 which shows particles containing Ti. However, SEM observations did not show any cube shaped TiN in the as-received samples. Figures 4 to 6 show the presence of Ti precipitates in a given sample heat treated at temperatures of 1130 °C, 1250 °C and 1400 °C respectively. They show that with increasing heat treatment temperature the content of the precipitates changes, with leaving only Ti and N at 1400 °C. Figure 7 shows TiN particles are precipitated after heating the sample to 1240 °C followed by oil quenching.

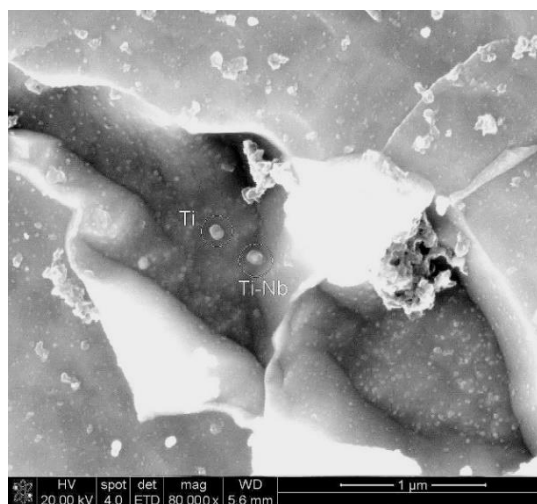
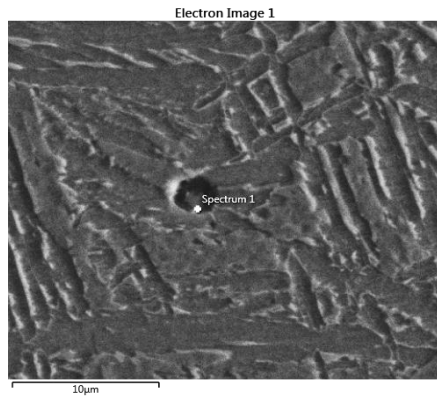


Figure 3: SEM micrograph showing Ti and Ti-Nb based particles in the as-received EH46.

277



278

279

280

281

282

283

284

285

286

287

288

289

290

291

292

293

294

295

296

297

298

299

300

301

302

303

304

305

306

307

308

309

310

311

312

313

314

315

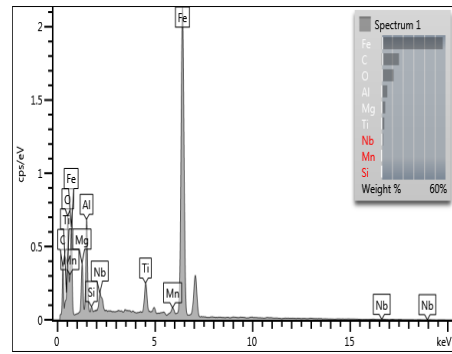
316

317

318

319

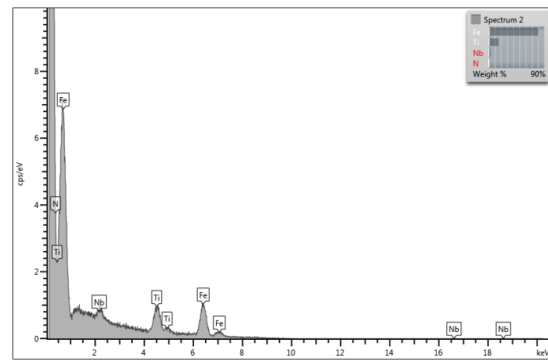
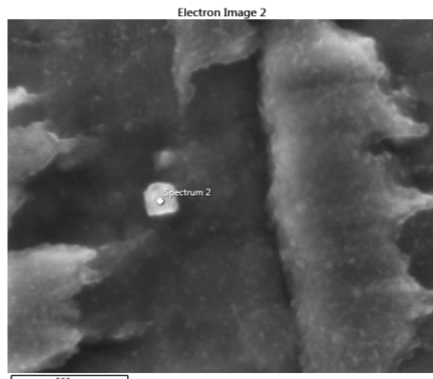
320



-a-

-b-

Figure 4: EH46 sample, heated to 1130 ° C for 1min, followed by hot oil quenching (30K/sec), a-SEM micrograph, -b-EDS spectrum of a particle in the heat treated sample showing Ti, Nb, Mn, Si, Al, Mg and Oxygen as its constituents.

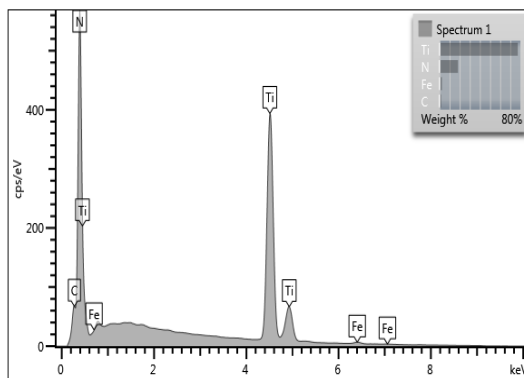


299

-a-

-b-

Figure 5: EH46 sample heated to 1250 ° C for 1min, followed by hot oil quenching (30K/sec), a-SEM micrograph, -b-EDS spectrum of a particle in the heat treated sample showing Ti, Nb and N as its constituents.



-a-

-b-

Figure 6: EH46 sample heated to 1400°C for 1min, followed by oil quenching (90K/sec), a-SEM micrograph, -b-EDS spectrum from a precipitate (of few microns) in the heat treated sample showing Ti and N as its constituents.

321
322
323
324
325
326
327
328
329
330
331
332
333
334
335
336
337
338
339
340
341
342
343
344
345
346
347
348
349
350
351
352
353
354
355
356
357
358
359
360
361
362
363
364
365
366
367
368

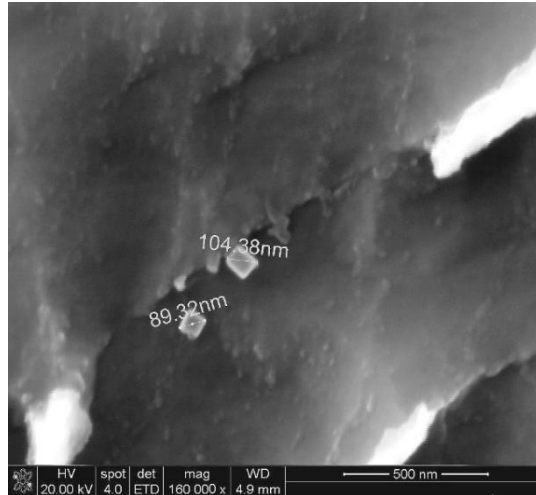


Figure 7: SEM micrograph of EH46 sample heated treated at 1240 °C, held for 1min followed by oil quenching (90K/sec). Photographs taken from different parts of the same sample show size of TiN particles varies between 0.09 and 0.3 µm (90 and 300 nm).

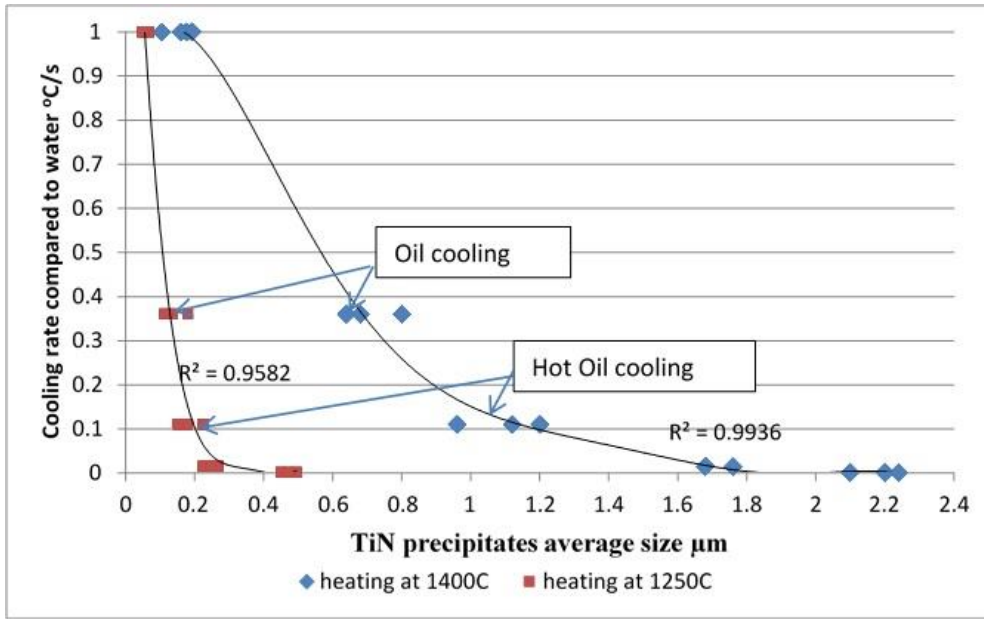
3.3 The Effect of the cooling rate on the size of TiN precipitates

To understand the effect of cooling rate on the size of TiN precipitates, unwelded samples of EH46 were heat treated at 1250 °C and 1400 °C and then were cooled at different cooling rates: oil quenching, hot oil quenching, air cooling and cooling inside furnace. Figures 8 and 9 show the relationship between the cooling rate and TiN particle size for samples heat treated at 1250 °C and 1400 °C with holding times of 10 sec and 30 secs, respectively. Comparing Figures 8 and 9 reveals 30 secs holding time results in larger size particles; however, the Figures show among the effect of temperature, holding time and cooling rate, cooling rate plays a more prominent role in the size of precipitates in the heat treated EH46 samples.

Additionally, Figure 10 presents the size distribution of TiN particles (µm) in the heat treated samples cooled with hot oil quenching. It compares TiN particles size and distribution for different regimes of heat treatment conducted at two different temperatures of 1250 and 1400 °C both held for two different holding times of 10 and 30 seconds. This Figure evidently shows heat treatment of up to 1400 °C has led to larger precipitates ranging from 0.6 to 1.60 µm compared with precipitates of 0.5 to 0.5 µm in heat treated samples at 1250 °C.

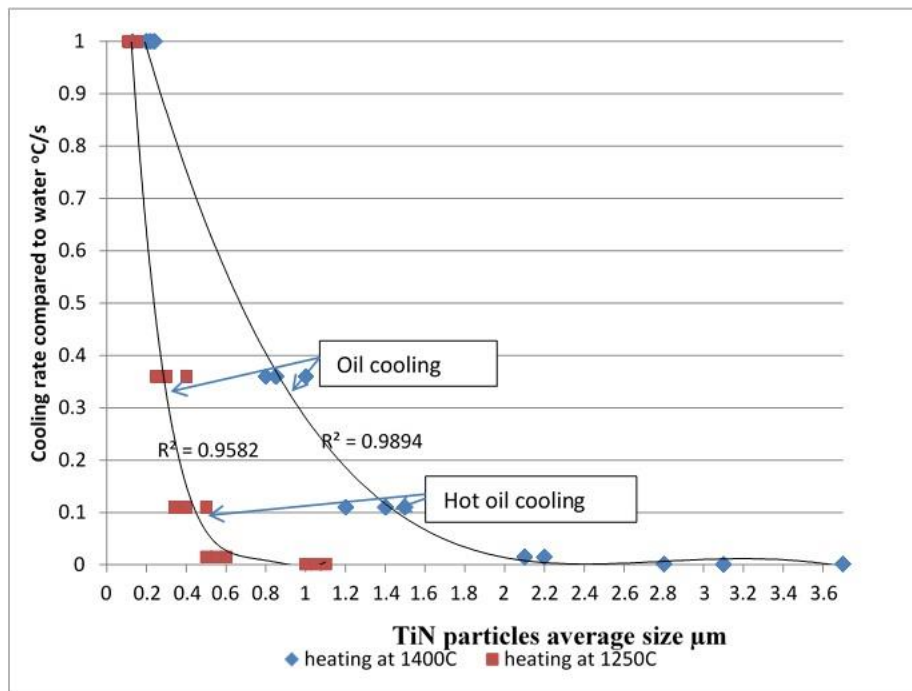
It is worth noting that, in a micro-alloyed steel, similar to this work, it has been shown that 10 seconds exposure to a high temperature has made a noticeable difference to the size and frequency of particles precipitating from the solid solution [16]. Hence, the importance of holding times as small as 10 seconds at temperatures above 1000 °C on the precipitates should not be ignored.

369
 370
 371
 372
 373
 374
 375
 376
 377
 378
 379
 380
 381
 382
 383
 384
 385
 386

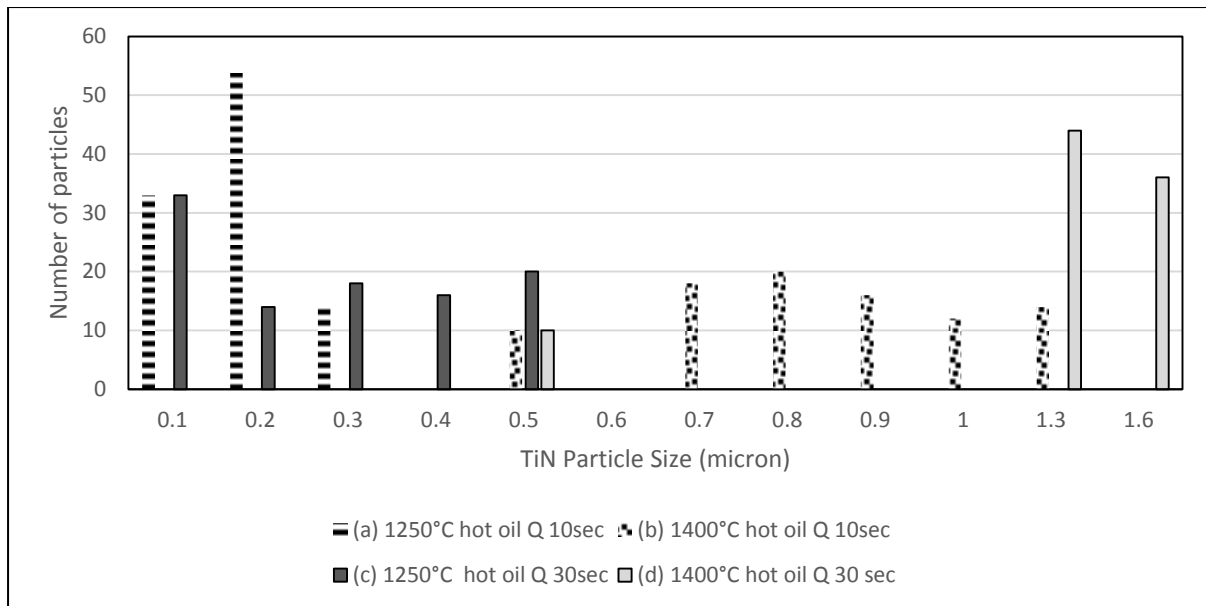


387 **Figure 8: The correlation between TiN precipitates size (in μm) and the cooling rate**
 388 **(K/s) (holding time was kept constant at 10 sec). It shows the size of precipitates**
 389 **increased with decreasing the cooling rate.**

390
 391
 392
 393
 394
 395
 396
 397
 398
 399
 400
 401
 402
 403
 404
 405
 406
 407
 408
 409



410 **Figure 9: The correlation between size of TiN precipitates (in μm) and the cooling rate**
 411 **in K/s (holding time was 30 sec), the size of precipitates increased with decreasing the**
 412 **cooling rate.**



413
414
415
416
417

Figure 10: Histogram showing the size distribution of TiN particles observed in the samples heated at different temperatures (and times) followed by hot oil quenching -a- 1250°C for 10 sec, -b-1400°C for 10 sec, -c-1250°C for 30 sec and -d-1400°C for 30 sec.

3.4 TiN precipitates in FS welded Samples of EH46

418 SEM-EDS were also carried out to reveal the TiN particles precipitated in FS welded joints
419 of EH46 steel. Given that FSW is a thermal process their particles size range was compared
420 with the heat treated (unwelded) samples. To compare the effect of welding traverse speed on
421 the constituents, Figure 11 -a- and -b- show high magnification micrographs of FSW EH46
422 W8 (150RPM, 50mm/min), whereas Figure 11 -c- and -d- show high magnification
423 micrographs of FSW EH46 W9 (150RPM, 100mm/min). They clearly illustrate that the
424 higher welding speed, traverse speed, (W9) resulted in finer precipitates with an average
425 particle size of 0.5 μm compared with 0.6 μm for W8. To study the plunge/dwell period
426 where there is no translational movement for FSW of EH46, Figure 12 shows high quantity
427 of large TiN particles at the plunge period for sample W9.

428 To understand the role of process parameters on TiN particle sizes, this work also looked at
429 the effect of tool rotational speed during plunge/dwell period which corresponds to the
430 beginning of the FSW where there are no translational movements. Figure 13 -a- and -b-
431 show TiN precipitates in EH46 W2 and W3 (plunge/dwell period) for region 1 (under tool
432 shoulder). They show W3 with lower rotational speed and slightly shorter dwell time,
433 contains smaller precipitates than W2 (0.5 μm compared with 0.7 μm).

434 Table 4 summarizes the TiN average particle size of EH46 W1 to W7 (plunge/dwell) at the
435 shoulder-probe region. The table presents higher values for average particle size in W1 and
436 W2, 0.6 and 0.7 μm respectively, compared with 0.5 μm for the remaining samples. This
437 means higher rotational speed results in larger TiN precipitates on average, due to higher heat
438 input.
439

440 To relate the role of FSW welding process parameters on particle frequency, in a histogram
441 format Figures 14a and 164 illustrate the frequency distribution (%) of the TiN particle with
442 varied size of 0.01 to 0.9 μm observed in W8 and W9 (steady state welding) and W1 to W7
443 (Plunge/Dwell), respectively. From comparing W8 and W9 in Figure 14a, clearly it can be
444 seen that W9 (with higher transverse speed) produces finer particles. Figure 14b reveals that
445 samples W3 to W7 present very similar particle distribution pattern. Given that they have
446 very similar process parameters, this shows the reproducibility of the data.
447

448
449
450
451
452
453
454
455
456
457
458
459
460
461
462
463
464
465
466
467
468
469
470
471
472
473
474
475
476
477
478
479
480
481
482
483
484
485
486
487
488
489
490
491
492
493
494
495
496
497

As an example, Figure 15 shows one TiN particle with a size of 0.35 μm under probe side of W2 (region 2). This is very small compared to precipitates observed in region 1 of the weld (Figure 13a: 0.7 μm). This confirms region 1 experiences higher peak temperature.

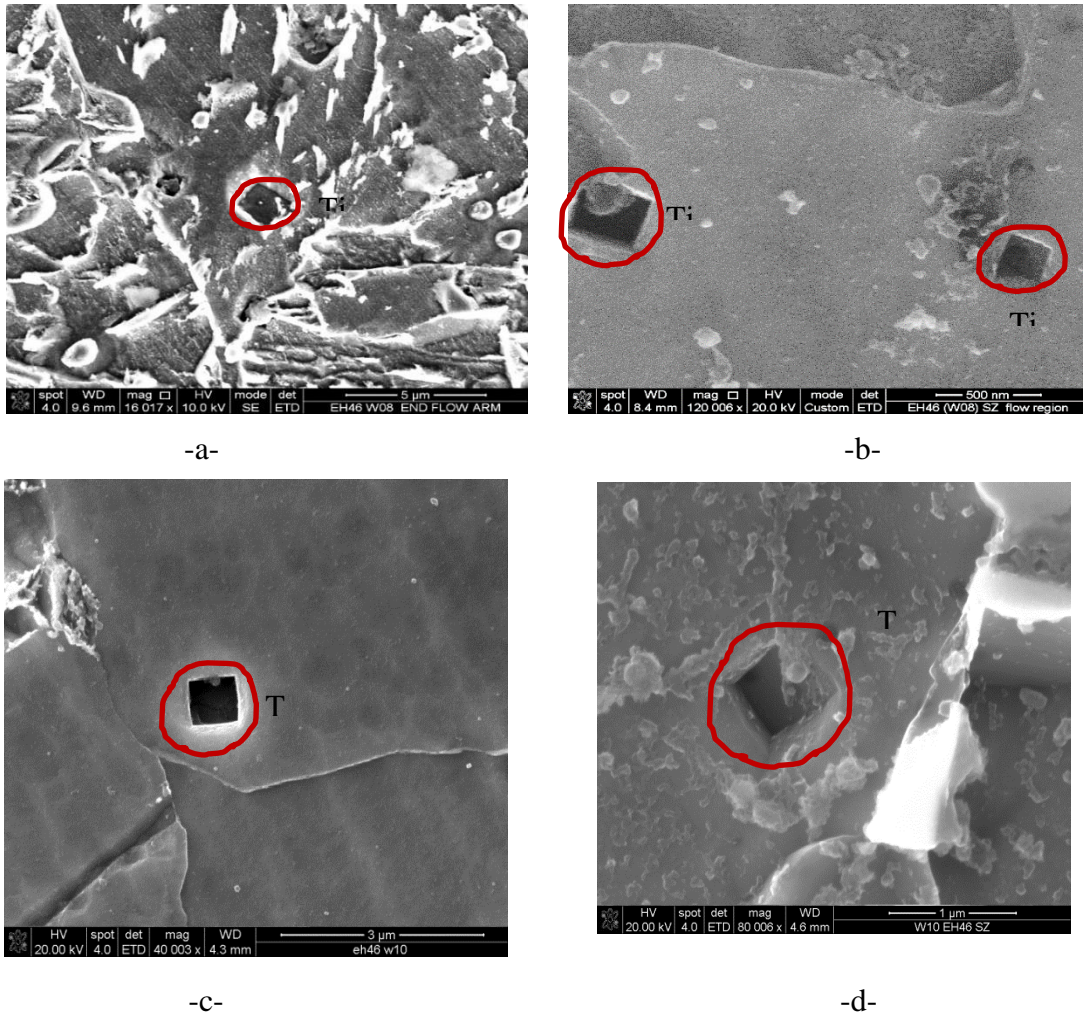
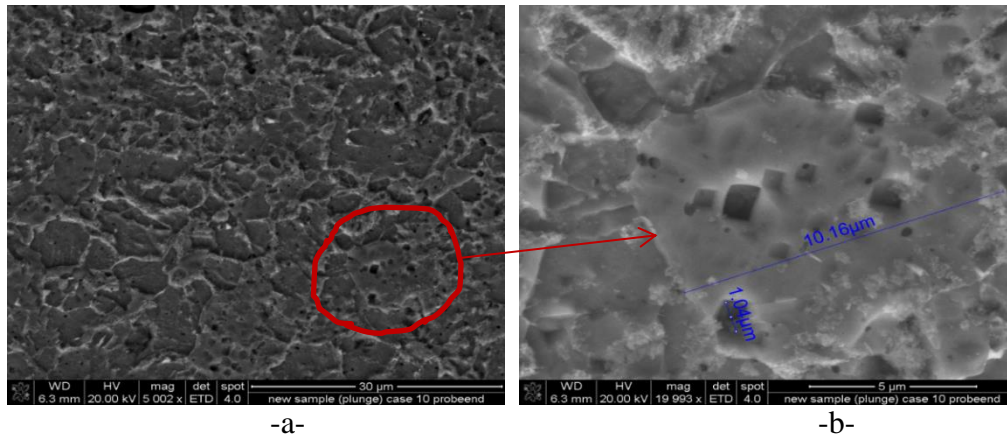


Figure 11: SEM micrographs of FSW EH46 samples -a- and -b- TiN particles in W8 (150RPM, 50mm/min), average size is 0.6 μm , -c- and -d- TiN particles in W9 (150RPM, 100mm/min), average size is 0.5 μm .

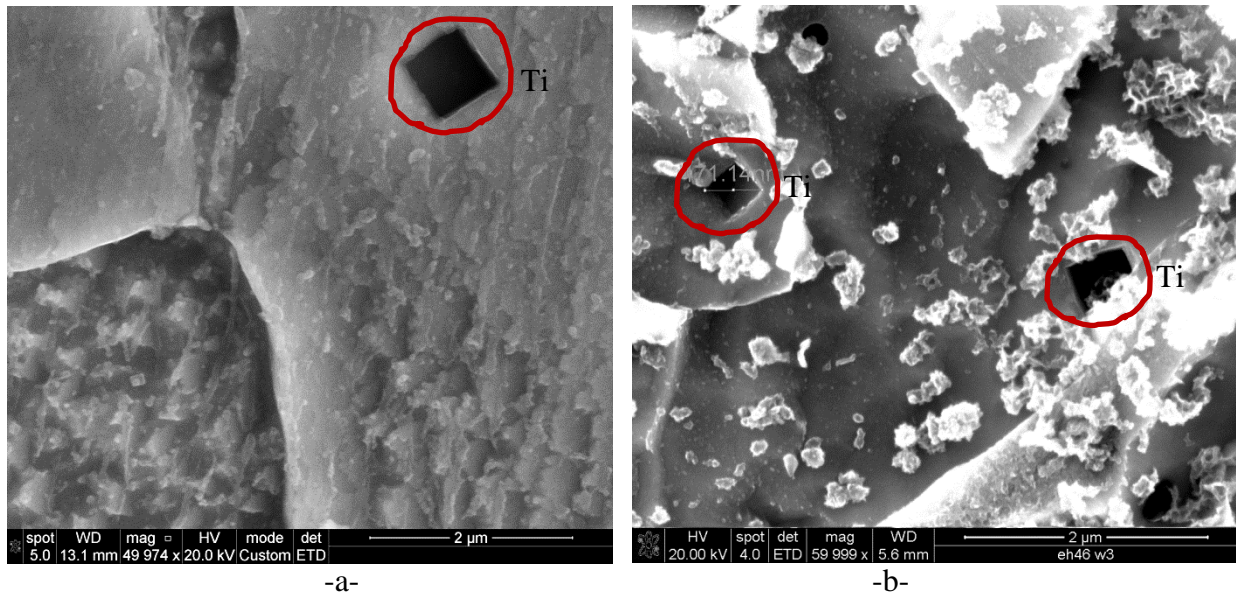
498
499
500
501
502
503
504
505



517

518 **Figure 12: SEM micrographs of EH46 W9 (during plunge/dwell period) probe-end, -a-**
519 **low and -b- high Magnifications, showing numerous TiN precipitates (size varies**
520 **between 0.7 to 1.5μm).**

521

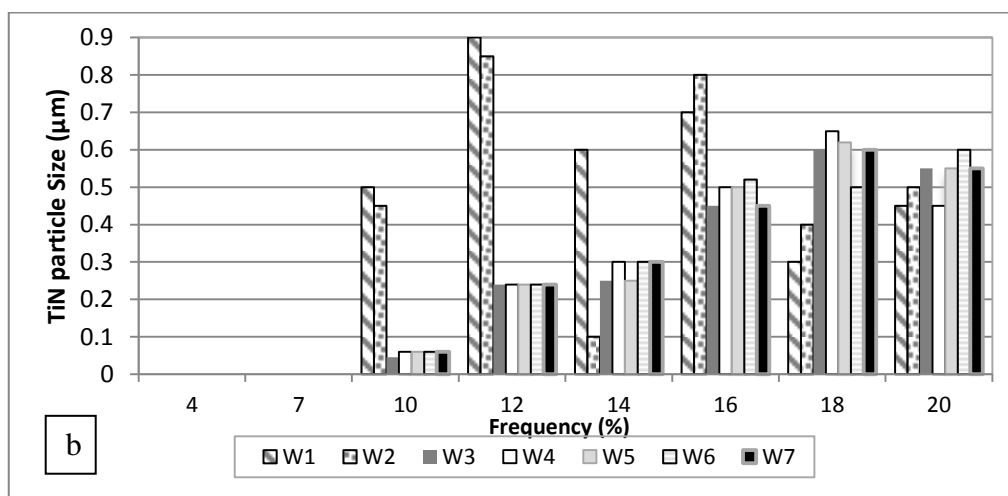
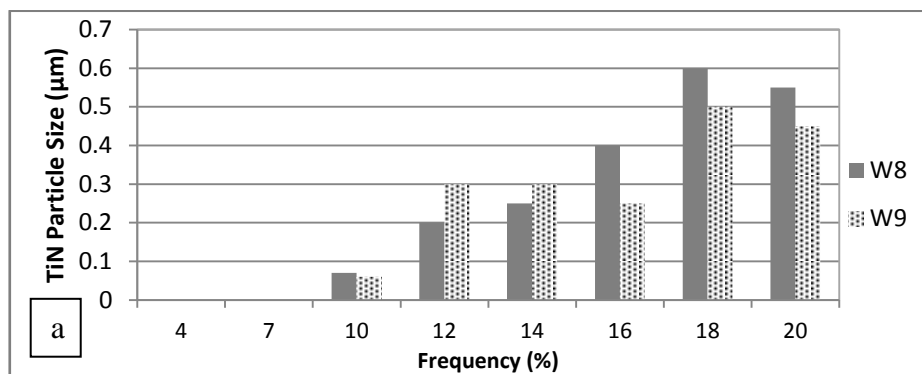


537

538 **Figure 13: SEM micrographs of EH46 (plunge/dwell period) region 1 under tool**
539 **shoulder -a-W2 with an average TiN particle size of 0.7μm, -b- W3, with an average TiN**
540 **particle size of 0.5μm.**

541
542
543
544
545
546
547

548
549



550
551 **Figure 14: The Frequency Distribution (%) of the TiN particle size (µm) observed in -a-**
552 **FSW EH46 W8 and W9 (steady state), -b- FSW EH46 W1 to W7 (Plunge/Dwell).**

553
554 **Table 4: TiN average particle size of samples W1 to W7 observed at the shoulder-probe**
555 **region (Region 1): (Standard deviation value= 0.05 µm)**

Weld No.	W1	W2	W3	W4	W5	W6	W7
TiN average particle size (µm)	0.6	0.7	0.5	0.5	0.5	0.5	0.5

556
557
558 **Table 5: Interaction coefficients in molten steel at 1600°C (1873K) [21].**

Element	C	Si	Mn	P	Al	Ti	N
e_{Ti}^J	-0.165	0.050	0.0043	-0.64	12	0.013	-0.018
e_N^J	0.130	0.047	-0.02	0.045	-0.028	-0.53	...

559
560
561
562
563
564

565
566
567
568
569
570
571
572
573
574
575
576
577
578
579
580
581
582

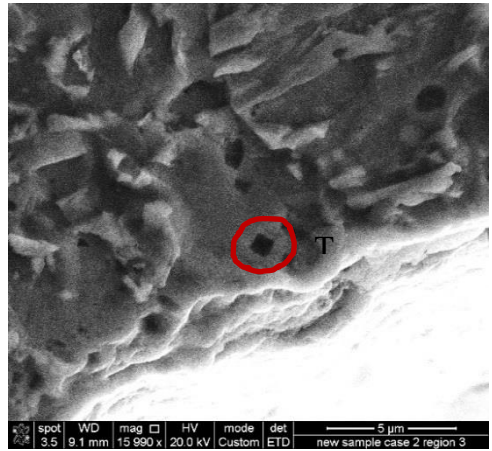
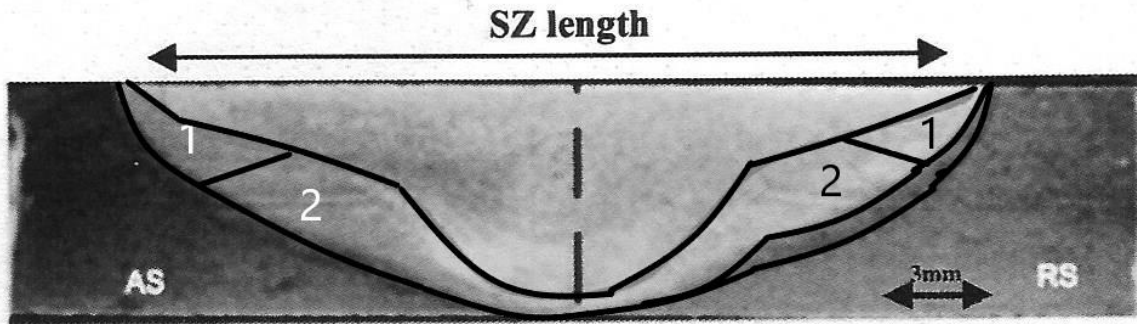


Figure 15: SEM Micrograph of sample W2 (plunge/dwell period) under the probe region showing TiN particles with average of 0.35 μm in size.



583
584
585
586
587
588

Figure 16. Two affected regions identified following the weld tool plunge trials sample W2, under the shoulder region (region 1) and around the probe side (region 2), both these regions are thermomechanically affected zones. Temperature predicted for region 1 to be reaching near 1400°C and for region 2 not to be greater than 1250°C.

589

4. Discussion:

590

4.1 Prior Austenite Grain Size (PAGS) and the effect of temperature

591
592
593
594
595
596
597
598
599
600
601
602
603
604
605

Figure 2 plots the correlation between PAGS and temperature for the heat treated samples heated in a temperature range of 1000 to 1400 °C at holding time of 30sec then cooled by oil quenching. As the Figure shows PAGS increases gradually with a rise in peak temperature of heat treatment; however, it increases at a higher rate when the heating peak temperature exceeds 1300-1400 °C. This is attributed to the role of Ti precipitates when exposed to high temperature heat treatment. Ti is proven to be a very effective element in controlling the austenite grain size and keeping it under 200μm when heated up to 1300°C. This is due to imposing of the pinning forces at the grain boundaries [17]. In a previous study in a low carbon HSLA steel, (0.165 C, 1.11 Mn, and 0.34 wt% Ni), using a simple carbides and nitrides model Fernandez et al [18] theoretically determined the solubility temperature of TiN to be around 1682°C. They studied the role of heat treatment on grain growth; given that their product was hot rolled, the grain growth began at lower temperatures and it was found that at short heat treatments (between 5 to 30 min) when the temperature exceeded 1200 °C a drastic grain growth was observed; however, for longer heat treatment this critical temperature was

606 lowered down to 1150°C. This was attributed to the dissolution of all carbides and nitrides
607 precipitates during heat treatment [18]. Similar to Fernandez et al [18], here PAGS, as shown
608 in Figure 2, was increased significantly after reaching temperature of 1300-1400 °C which
609 can indicate that most of particles responsible for grain refining by the effect of force pinning
610 have been dissolved. It is worth noting that a study by Karmakar et al. [19] on the effects of
611 microalloyed elements on PAGS has shown that Ti-Nb elements are the most effective
612 elements in pinning the austenite grains when heat treated. Similar to this work, they reported
613 that grain growth of austenite can occur when the temperature exceeds 1150 °C as a result of
614 Ti-Nb dissolution. However, the abnormal grain growth in austenite was reported to occur
615 slightly at higher temperature than here, after reaching a temperature of 1400 °C due to
616 complete dissolution of TiN particles.

617 It is worth noting that here only the role of temperature on pinning effect of TiN precipitates
618 is taken into account and not the role of deformation and the introduction of stress and
619 therefore, strain. Deformation leads to recovery and/or recrystallization which results in
620 softening. However, small precipitates can delay the recovery and recrystallization and
621 therefore, grain growth can be prohibited or delayed if strain is low; however, at higher
622 strains they become less effective due to increased rate of recovery and recrystallization. This
623 means increasing the amount of deformation leaves a very limited time for nucleation of
624 precipitates. Some measurements of such behavior can be found elsewhere [20].
625

626 **4.2. Thermodynamics of TiN formation in low alloy steel**

627 Precipitation behavior of TiN in low alloy steels during solidification and hot rolling (hot
628 deformation) are carefully studied, this is done through application of current chemical
629 content to thermodynamics formulae relevant to this grade.

$$630 \quad [Ti] + [N] = TiN (s), \Delta G = \Delta G^\theta + RT \ln \frac{1}{f_{Ti} \cdot [Ti] \cdot f_N \cdot [N]} \quad (2)$$

$$631 \quad \Delta G^\theta = -291000 + 107.91 T \quad (3)$$

632 where f_{Ti} and f_N are the activity coefficient of Ti and N in molten steel, respectively [21].
633 The activity coefficients of Ti and N can be obtained using the following equations, chemical
634 content of the steel and the interaction coefficient values of each element in the molten steel
635 listed at Table 5.
636

$$637 \quad \lg f_{Ti} = \left(\frac{2557}{T} - 0.365 \right) \sum \left(e_{Ti(1873K)}^j [\%j] \right) \quad (4)$$

$$638 \quad \lg f_N = \left(\frac{3280}{T} - 0.75 \right) \sum \left(e_{N(1873K)}^j [\%j] \right) \quad (5)$$

639 Using equations 2 to 5 and data in Tables 1 and 5 results in Gibbs free energy equation for
640 dissolution of TiN in the studied alloy as follows:

$$641 \quad \Delta G = -291000 + 181.996T \quad (6)$$

642 When the reaction reaches equilibrium that $\Delta G=0$ and therefore $T= 1325.94^\circ\text{C}$. Therefore,
643 based on these calculations for TiN to precipitate at this alloy temperature must reach about
644 1326°C . This calculation does not take into account the role of hot deformation in inducing
645 precipitates, but as discussed in the above section this won't be significant.
646

647

648 **4.3 TiN precipitates in the heat treated samples**

649 Samples which were heat treated at 1000 °C did not show evidence of TiN precipitates under
650 the SEM investigation. This can be due to the fact that the TiN precipitation usually occurs at
651 temperatures exceeding 1000 °C [12]. Other samples which experienced higher temperatures
652 showed different size of Ti precipitates including TiN shown in SEM images and EDS
653 spectrum in Figures 4 to 6. In this work, heating up to 1130°C with different cooling rates

654 resulted in precipitation of Ti with other elements including Al, Nb, S, O, V, P as shown in
655 Figure 4. The current work is only focused on TiN precipitates and thus the other Ti
656 precipitates will not be discussed. Samples heated at 1240°C (Figure 5) had TiN precipitation
657 with average size of 0.1µm (100nm) accompanied with Nb whereas, heating up to 1400°C
658 resulted in a coarser precipitation of TiN (0.5-1µm) as shown in Figure 6. Cooling of samples
659 presented in Figures 4 to 6 was achieved by quenching in hot oil of temperature of 100°C;
660 this produced a cooling rate of 30°C/sec which is the expected cooling rate that produces a
661 ferrite/ cementite aggregate microstructure [22] similar to the FSW samples microstructure
662 observed in this work. This suggests the cooling rate of FSW samples would have been close
663 to this rate. Ti usually has a strong affinity to form nitrides, oxides and even sulphides before
664 forming carbides [23], adding elements forming nitrides (e.g. V, Ti) to steel leads to the
665 precipitation of pure V (or Ti) nitrides and thermal stability of nitrides is higher compared to
666 equivalent carbides [24]. It is known that pure TiN requires low amount of Ti in the steel
667 matrix (less than 0.025wt%) and also low carbon content, otherwise other precipitates such
668 as (Mn, Ti)S or Ti (C,N) will be more dominant precipitate depending on the composition of
669 steel [25-26].
670

671 **4.4 The Effects of the cooling rate on TiN particle size**

672 Figures 8 and 9 show the relationship between the cooling rate and the average size of TiN
673 particles for two different heat treatment temperatures and two different holding times. The
674 TiN particle size increases significantly when cooling rate decreases, especially when
675 samples cooled inside a furnace. It is evident that TiN can precipitate even under a fast
676 cooling regime such as oil quenching. A work carried out on low carbon steel (0.12-0.14%C)
677 with a Ti% 0.006-0.013 [8] showed that cubic TiN can be precipitated after heating up to
678 1526°C where there were no pre-existing TiN precipitates and then cooling down to 1000°C
679 at various cooling rates. However, compared to this work, in their case precipitates were very
680 small and were formed as clusters of particles [8]. This suggests that the temperature, i.e. heat
681 treatment temperature is a key factor in forming the precipitates rather than the cooling rate.
682 The cooling rate only influenced the size and frequency of the precipitates but not their
683 occurrence and formation.

684 The slower cooling rate means that the TiN precipitates can nucleate in longer period at
685 temperature and thus leads to coarsening of the precipitates. This has been observed
686 previously [9] where it is shown that in addition to heating and cooling conditions,
687 interactions between steel composition and processing were also significant factors in TiN
688 precipitates size and distribution. It is concluded that final particle size is influenced by a
689 competition between coarsening and completion of precipitation.

690 Increasing the holding time to 30 sec at 1400°C with a very slow cooling rate (cooling inside
691 a furnace) has resulted in coarsening of TiN particles exhibiting particles exceeding 3µm in
692 size, as shown in Figures 9 and 10 d. The faster cooling rate can lead to a larger undercooling
693 and higher supersaturating of solute for precipitation and thus larger driving force, so more
694 fine particles will form at lower temperature. Figure 10 shows the size frequency (%) of TiN
695 particles when heating to 1250 and 1400 °C both for 10 and 30 secs. The Figure shows TiN
696 particle size increased with an increase in the temperature, the frequency of large particle size
697 also increased when soaking time increased. This was due to formation of more TiN
698 precipitates. With holding longer at the temperature, precipitate nucleation may occur over a
699 prolonged period and hence it is possible for small particles nucleated later to co-exist with
700 larger particles that formed earlier. This leads to particle size variation as shown in Figure 10.
701

702

703

703 **4.5 TiN precipitates in FSW samples of EH46**

704 SEM micrographs of EH46 FSW samples (W8 and W9) exhibit precipitations of TiN in the
705 top of the stir zone (SZ) with average size of 0.6 μm (600nm) and 0.5 μm (500nm) in the
706 steady state period as shown in Figures 11 a to d, respectively. The TiN particle size
707 exceeded 1 μm in the plunge period (the start of welding where the tool is rotating but not
708 moving) as shown in Figures 12 a and b. In these Figures, eight TiN particles (size is 0.7 μm
709 to 1.5 μm) can be counted inside a 10 μm ferrite grain. This coarsening of TiN particles is
710 believed to be resulted from exposure to high temperature and slow cooling rate.
711 The plunge/dwell cases of EH46 W1 to W7 have also been investigated for TiN precipitates,
712 Figures 13 a and b show TiN precipitates of W2 and W3 respectively at region 1 under tool
713 shoulder. An average size of 0.70 and 0.5 μm is calculated for particles in region 1 of W2 and
714 W3, respectively. The average size of TiN particles is calculated and listed at Table 4 (with
715 an accuracy of $\pm 0.05 \mu\text{m}$). Figure 15 shows TiN particle at region 2 under tool probe with
716 average size of 0.35 μm . This decrease in TiN particle size from 0.70 μm to 0.35 μm can be
717 attributed to a lower peak temperature under probe (region 2) compared to the region under
718 shoulder (region 1).

719

720 **4.6 Comparison of FSW and heat treatments in terms of TiN Precipitation**

721 As shown in Figure 10 it is evident that heat treatments at 1250 $^{\circ}\text{C}$ followed by hot oil
722 quenching resulted in TiN precipitates with size of 0.2 to 0.5 μm similar to W9 sample,
723 which contains TiN precipitates of almost the same size and frequency (Figure 14a). W8
724 shows coarser TiN particles with average of 0.6 μm which suggests slower cooling rate than
725 in W9 as the tool traverse speed was halved the speed of W9. Cooling rate is estimated to be
726 in the range of 10 to 30 K/s based on the comparison with results of heat treatments with a
727 minimum peak temperature of 1250 $^{\circ}\text{C}$. The ferrite grain shown in Figure 12 with average
728 grain size of 10 μm contains eight large cubic precipitates of TiN which are ranging from 0.7
729 to 1.5 μm . The large size of these precepitates indicates that the material has been exposed to
730 a very high temperature (may have reached 1400 $^{\circ}\text{C}$, the cooling rate was slow enough to
731 form these precipitates, expected less than 10K/s). It is, however, unlikely these large
732 precipitates can play any significant role in pinning the austenite grain during heating. The
733 reduction in pinning forces due to temperature increase higher than 1200 $^{\circ}\text{C}$ was reported by
734 Karmaker et al. [19] and also by Gong et al. [16] where the austenite grains experienced
735 coarsening resulted from Ti-Nb dissolution. Therefore, similarly, the coarse ferrite grain at
736 the probe end of W9 during the plunge period shown in Figure 12 which exceeds 10 μm can
737 be attributed to the loss of the pinning force of precipitates, in addition to the high
738 temperature and slow cooling rate. As discussed in section 4.1 grain growth could also be
739 attributed to the role of deformation through increased rate of recovery and recrystallisation
740 and not only the removal of pinning effect.

741 In the plunge cases of W1 to W7 SEM examinations have shown occurrence of TiN
742 precipitation in the shoulder-probe region (as shown in Figure 13). The average size of these
743 precipitates are summarised and presented in Table 4. The table shows W1 and W2 exhibit
744 larger average size of TiN particles (0.6-0.7 μm) than other samples, W3 to W7 (0.5 μm).
745 This has been attributed to having higher tool rotational speed (200RPM) for W1 and W2
746 compared to other welds which have a lower tool rotational speed (120RPM). The higher tool
747 speed could have caused higher peak temperature and thus slower cooling rate expected. This
748 in turn can lead to TiN particle coarsening as discussed previously. The temperature of W1
749 and W2 at the shoulder-probe is expected to exceed 1250 $^{\circ}\text{C}$ but not to reach 1400 $^{\circ}\text{C}$
750 according to the heat treatments results shown in Figures 8 and 9. W3 to W7 peaks
751 temperatures are expected to reach 1250 $^{\circ}\text{C}$ with a cooling rate range of 20 to 30K/s.

752 Figure 15 shows TiN particle at the probe side of W2, the average calculated size of TiN
753 particles was 0.35 μm which is smaller than that found at the shoulder-probe region. The

754 reduction in TiN particles size can be attributed to a lower peak temperatures and faster
755 cooling rate. This result agrees with previous works [27-29] that shows that heat generation
756 in FSW is spatial and the maximum temperature is always at the tool/workpiece contact
757 region.

758 Figure 16 illustrates the temperature distribution under the tool based on temperature
759 predictions made here for one of the samples (W2).

760 As shown understanding TiN formation during heat treatments can be a very useful method
761 in estimating peak temperature and cooling rate of the FSW joints of EH46 steel and thus can
762 assist with determining suitable rotational and traverse speeds of the tool to produce sound
763 joints without a need for using thermocouples or thermal imaging camera. But it is worth
764 noting that FSW is not purely a thermal process and as a result some of precipitates may have
765 been strain induced. However, this has not been evidently proven. It is known that diffusivity
766 of Ti must be sufficient for the TiN precipitates to grow or coarsen. Additionally, the
767 presence of dislocations and grain boundaries which have an impact on the diffusion can play
768 an important role. It is previously shown that an increase in atom mobility due to the defect
769 presence results in faster Ostwald ripening of the existing particles [30]. It is also shown [9]
770 that deformation increased dislocation densities and hence assisted diffusion mechanism.
771 Deformation could also move jog-dragging screw dislocations, and hence a line of vacancies
772 in the matrix can be formed. This itself can enhance bulk diffusion and assist with Ostwald
773 ripening. Based on the above, “deformation enhanced coarsening” can be a possible
774 mechanism for some drastic increase in particle size experienced after rolling in steel [31].
775 However, there has not been any work demonstrating the role of deformation/ strain leading
776 to a significant change in formation temperature of TiN precipitates in steel. This suggests the
777 present work which has only taken thermal process into effect is not very unrealistic and
778 hence can provide a rather good estimation for peak temperature and cooling rate in FSW of
779 EH46 steel.

780

781 **Conclusions**

782

783 The work presented is the first attempt to estimate the temperature in the stirred zone and
784 cooling rate of FSW of steel joints from precipitates formed after welding. After undertaking
785 a series of heat treatments to produce varied temperature and cooling rate conditions, the
786 work compared the heat treated samples with samples welded using Friction Stir Welding
787 technique with few different welding variables in EH46 steel samples. It looked at the role of
788 rotational speed and traverse speed on the peak temperature at the tool/joint interface. From
789 the results the following conclusions can be drawn:

790 1. Prior Austenite grains coarsened dramatically when heating temperature of unwelded
791 samples exceeded 1300-1400°C. This was attributed to the reduction in pinning forces resulted
792 from the dissolution of Ti/ Ti-Nb based particles and formation of new coarse cubic
793 precipitates of TiN. Thermodynamic calculations estimated the dissolution temperature of
794 TiN to be ~1326°C.

795 2. It is found that the temperature at the weld/tool interface is the main driver for TiN
796 formation, and TiN begins to precipitate when the sample temperature exceeds 1100°C. Pure
797 TiN can precipitate at high temperatures in the range of 1250 -1400°C. However, their size
798 was also influenced by the cooling rate and the soaking time. This was more profound at
799 higher heat treatment temperatures.

800 3. The average size of TiN particles increased with decreasing cooling rate, a maximum
801 precipitate size which exceeded 3µm was found when unwelded EH46 samples heated to
802 1400°C and then cooled slowly inside a furnace with a cooling rate of 0.35 K/s.

803 4. When EH46 heated to two different temperatures of 1250 and 1400°C followed by cooling
804 at different cooling rates quenching in oil (90K/sec), quenching in hot oil with a temperature
805 of 150°C (30K/sec), still air cooling and cooling inside a furnace (0.35K/sec) and held at two
806 different holding times of 10 and 30 secs, it is found that the cooling rate, and not the
807 temperature, played a prominent role in forming smaller precipitates at higher cooling rates
808 (0.2-0.4 µm for cooling with a rate of 240K/sec). However, in lower cooling rates such as
809 cooling in furnace heat treatment had more profound effect; i.e. lower heat treatment
810 temperature led to smaller size precipitates.

811 5. Using this new technique for samples FS welded (plunge and dwell stage) under two
812 different rotational speeds of 120 and 200 RPM revealed the temperature in their stirred zone
813 is to be approximately 1250 and 1400°C, respectively. For samples welded under rotational
814 and traverse speeds of 150 RPM and 50 mm/min the temperature in the stirred zone is to be
815 approximately 1400°C.

816 Overall, it is shown to estimate the peak temperature of weld/joint interface and associated
817 cooling rate for Friction Stir Welding from TiN precipitates and their size distribution
818 provides a valid basis for an inexpensive method to replace other technique such as utilization
819 of thermocouples or thermal imaging cameras.

820
821

822 **Acknowledgement**

823 The authors would like to thank The Welding Institute (TWI) Yorkshire for providing FSW
824 samples of steel and related operational data, also special thanks to Mr Stuart Creasy at
825 Sheffield Hallam University for helping in obtaining clear SEM images at high magnification.

826
827

828 **References**

- 829 1. W.M. Thomas, E.D. Nicholas, J.C. Needham, M.G. Murch, P. Templesmith and C.J. Dawes:
830 Friction Stir Butt Welding, International Patent No. PCT/GB92/02203 (1991).
- 831 2. S.A. Hussein, S. Thiru, R. Izamshah and A.S.M.D. Tahir: *Advances in Mat. Sci. & Eng.*, 2014, 8
832 pages.
- 833 3. P. Carlone and G.S. Palazzo: *Metallogr. Microstruct. Anal.*, 2013, vol. 2, pp. 213-222.
- 834 4. J. Mezyk and S. Kowieski: *Solid State Phenomena*, 2015, vol. 220-221, pp. 859-863.
- 835 5. Z.H. Zhang, W.Y. Li, J.L. Li and Y.J. Chao: *Int. J. Adv. Manuf. Technol.*, 2014, vol. 73, pp. 1213-
836 1218.
- 837 6. A. Arora, T. DebRoy and K.H.D.H. Bhadeshia: *Acta Mater.*, 2011, vol. 59, pp. 2020-2028.
- 838 7. L. Wang, C.M. Davies, R.C. Wimpory, L.Y. Xie and K.M. Nikbin: *Materials at High Temperature*,
839 2010, vol. 27, pp. 167-178.
- 840 8. J. Stock, C.M. Enloe, R.J. O'Malley, and K.O. Findley: *AIST Transactions*, 2014, vol. 11, pp. 180-
841 186.
- 842 9. M.T. Nagata, J.G. Speer and D.K. Matlock: *Metall. Mater. Trans. A*, 2002, vol. 33A, pp. 3099-
843 3110.
- 844 10. K.A. EL-Fawakhry, M.F. Mekkawy, M.L. Mishreky, and M.M. Eissa: *ISIJ International*, 1991,
845 vol. 31, pp. 1020-1025.
- 846 11. M.L. Wang, G.G. Cheng, S.T. Qiu, P. Zhao, and Y. Gan: *International Journal of Minerals,*
847 *Metallurgy and Materials*, 2010, vol.17, pp. 276-281.
- 848 12. S.G. Hong, H.J. Jun, K.B. Kang and C.G. Park: *Scr. Mater.*, 2003, vol. 48, pp. 1201-1206.
- 849 13. D.M. Failla, 2009, Friction Stir Welding and Microstructure Simulation of HSLA-65 and
850 Austenitic Stainless Steels, MSc Thesis, The Ohio State University.
- 851 14. S.F. Medina, A. Quispe and M. Gomez: *Metall. Mater. Trans. A.*, 2014, vol. 45A, pp. 1524-1539.
- 852 15. Z.H. Zhu and S.T. Qiu: *Advanced Materials Research*, vols. 535-537, pp. 633-638.
- 853 16. P. Gong, E.J. Palmiere and W.M. Rainforth: *Acta Mater.*, 2015, vol. 97, pp. 392-403.

- 854 17. L.J. Cuddy: “The Effect of Microalloy Concentration on the Recrystallization of Austenite During
855 Hot Deformation”, In: A. J. DeArdo, G. A. Ratz, and P. J. Wray, eds. Thermomechanical processing
856 of microalloyed austenite. Pittsburgh, USA: TMS-AIME, 1981: 129-140.
- 857 18. J. Fernández, S. Illescas and J.M. Guilemany: *Mater. Letters*, 2007, vol. 61, pp. 2389–2392.
- 858 19. A. Karmakar, S. Kundu, S. Roy, S. Neogy, D. Srivastava and D. Chakrabarti: *Mater. Sci. Tech.*,
859 2014, vol. 30, pp. 653-664.
- 860 20. J. Kunze, C. Mickel, G. Backmann, B. Beyer, M. Reibold, C. Klinkenberg, *Steel Research*, 1997,
861 vol. 68 (10), pp. 441-449.
- 862 21. T-P Qu, J. Tian, K-I Chen, Z Xu, D-Y Wang: *Ironmaking & Steelmaking*, 2019, vol. 46 (4), pp.
863 353-358.
- 864
- 865 22. S.F. Di Martino and G. Thewlis: *Metall. Mater. Trans. A.*, 2014, vol. 45A, pp. 579-594.
- 866 23. A.J. DeArdo: *International Materials Reviews*, 2003, vol. 48, pp. 371–402.
- 867 24. G. Stein, W. Kirschner and J. Lueng, Application of Nitrogen-Alloyed Martensitic Stainless Steels
868 in the Aviation Industry, 1997, Eds: E.G. Nisbett and A.S. Melilli , *Steel Forgings: Second volume*,
869 ASTM Special Technical Publication, pp104-115.
- 870 25. T. Shiraiwa and N. Fujino, “Electron Probe Microanalysis of Ti(C, N) and Zr(C, N) in Steel”,
871 1969, In: Möllenstedt G., Gaukler K.H. (eds) *Vth International Congress on X-Ray Optics and*
872 *Microanalysis*, Springer, Berlin, Heidelberg, pp 531-534.
- 873 26. M. Hua, C.I. Garcia, and A.J. DeArdo: *Metall. Mat. Trans. A*, 1997, vol. 28A, pp. 1769-80.
- 874 27. H. Schmidt and J. Hattel: *Modelling and Simulation in Materials Science and Engineering*, 2005,
875 vol. 13, pp.77–93.
- 876 28. H.B. Schmidt and J.H. Hattel: *Scripta Mater.*, 2008, vol. 58, pp.332–337.
- 877 29. P.A. Colegrove, H.R. Shercliff and R. Zettler: *Science and Technology of Welding and Joining*,
878 2007, vol. 12, pp. 284-297.
- 879 30. R.K. Gibbs, R.C. Peterson and B.A. Parker: *Proc. Int. Conf. on Processing, Microstructure and*
880 *Properties of Microalloyed and Other Modern High Strength Low Alloy Steels*, Iron and Steel Society,
881 Warrendale, PA, 1992, pp. 201-207.
- 882 31. S. Matsuda and K. Okumura: *Trans. Iron Steel Inst. Jpn.*, 1978, vol. 18, p. 198.

883
884

885 **List of Figures:**

886 Figure 1: Representation of the positioning of the seven plunge trials for EH46 steel plates.

887

888 Figure 2: Variation of prior austenite grain size with temperature for heat treated samples of
889 EH46 in temperature range of 1000-1500°C with holding time of 30sec.

890 Figure 3: SEM micrograph showing Ti and Ti-Nb based particles in the as-received EH46.

891 Figure 4: EH46 sample, heated to 1130°C for 1min, followed by hot oil quenching (30K/sec),

892 a-SEM micrograph, -b-EDS spectrum of a particle in the heat treated sample showing Ti, Nb,

893 Mn, Si, Al, Mg and Oxygen as its constituents.

894

895 Figure 5: EH46 sample heated to 1250°C for 1min, followed by hot oil quenching (30K/sec),

896 a-SEM image, -b-EDS spectrum of a particle in the heat treated sample showing Ti, Nb and

897 N as its constituents.

898

899 Figure 6: EH46 sample heated to 1400°C for 1min, followed by oil quenching (90K/sec), a-

900 SEM image, -b-EDS spectrum from a precipitate (of few microns) in the heat treated sample

901 showing Ti and N as its constituents.

902

903 Figure 7: SEM micrograph of EH46 sample heated treated at 1240°C, held for 1min followed

904 by oil quenching (90K/sec). Photographs taken from different parts of the same sample shows

905 size of TiN particles varies between 0.09 and 0.3 μm (90 and 300 nm).

906
 907
 908
 909
 910
 911
 912
 913
 914
 915
 916
 917
 918
 919
 920
 921
 922
 923
 924
 925
 926
 927
 928
 929
 930
 931
 932
 933
 934
 935
 936
 937
 938
 939
 940
 941
 942
 943
 944
 945
 946
 947
 948
 949
 950
 951
 952
 953

Figure 8: The correlation between size of TiN precipitates (in μm) and the cooling rate in K/s (holding time was 10 sec), the size of precipitates increased with decreasing the cooling rate.

Figure 9: The correlation between size of TiN precipitates (in μm) and the cooling rate in K/s (holding time was 30 sec), the size of precipitates increased with decreasing the cooling rate.

Figure 10: Histogram showing the size distribution of TiN particles observed in the samples heated at different temperatures (and times) followed by hot oil quenching -a-1250°C for 10 sec, -b-1400°C for 10 sec, -c-1250°C for 30 sec and -d-1400°C for 30 sec.

Figure 11: SEM micrographs of FSW EH46 samples -a- and -b- TiN particles in W8 (150RPM, 50mm/min), average size is 0.6 μm , -c- and -d- TiN particles in W9 (150RPM, 100mm/min), average size is 0.5 μm .

Figure 12: SEM micrographs of EH46 W9 (during plunge/dwell period) probe-end, -a-low and -b- high Magnifications, showing numerous TiN precipitates (size varies between 0.7 to 1.5 μm).

Figure 13: SEM micrographs of EH46 (plunge/dwell period) region 1 under tool shoulder -a- W2 with an average TiN particle size of 0.7 μm , -b- W3, with an average TiN particle size of 0.5 μm .

Figure 14: The Frequency Distribution (%) of the TiN particle size (μm) observed in -a- FSW EH46 W8 and W9 (steady state), -b- FSW EH46 W1 to W7 (Plunge/Dwell).

Figure 15: SEM Micrograph of sample W2 (plunge/dwell period) under the probe region showing TiN particles with average of 0.35 μm in size.

Figure 16. Two affected regions identified following the weld tool plunge trials sample W2, under the shoulder region (region 1) and around the probe side (region 2), both these regions are thermomechanically affected zones. Temperature predicted for region 1 to be reaching near 1400°C and for region 2 not to be greater than 1250°C.

Table 1: Chemical composition (wt%) of EH46 Steel Grade as received (composition is provided by the manufacturer).

C	Si	Mn	P	S	Al	N	Nb	V	Ti
0.20	0.55	1.7	0.03	0.03	0.015	0.02	0.03	0.10	0.02

954
955
956
957
958
959
960
961
962
963
964
965
966
967
968

Table 2: The welding parameters for FS welded EH46 plunge/dwell samples (W1-W7).

Weld Trial No.	Tool rotational speed ω (RPM) at dwell period	Max. Axial force (Plunge) (F_z) KN	Max. longitudinal force (F_x) KN	Max. Torque (M) N.m	Plunge Depth (Z) mm from FSW machine	Dwell Time (t) sec at dwell period
W1	200	157	17	498	13	6
W2	200	127	17	471	13	8
W3	120	116	21	598	13	7
W4	120	126	20	549	13	6
W5	120	115	17	532	13	7
W6	120	105	18	583	13	7
W7	120	119	20	548	13	7

969
970
971
972
973

Table 3: Welding parameters for FS welded EH46 steel at steady state condition (W8 and W9).

Weld No.	Tool rotational speed RPM	Traverse speed mm/min	Rotational/ Traverse speeds (rev/mm)	average spindle Torque N.m	average tool Torque N.m	Axial force (average) KN	longitudinal force (average) KN	Representation of Heat Input $(\frac{\omega \times \text{torque}}{v})$ (rev. KN)
W8	150	50	3	300	114	66	13	342
W9	150	100	1.5	450	171	72	14	256.5

974
975
976
977

Table 4: TiN average particle size of samples W1 to W7 observed at the shoulder-probe region (Region 1). (Standard deviation value= 0.05 μm)

Weld No.	W1	W2	W3	W4	W5	W6	W7
TiN average particle size (μm)	0.6	0.7	0.5	0.5	0.5	0.5	0.5

978

979 Table 5: Interaction coefficients in molten steel at 1600°C (1873K) [21].

Element	C	Si	Mn	P	Al	Ti	N
e_{Ti}^J	-0.165	0.050	0.0043	-0.64	12	0.013	-0.018
e_N^J	0.130	0.047	-0.02	0.045	-0.028	-0.53	...

980
981